Check for updates

NANO · MICRO small
www.small-journal.com

An ITO-Free Kesterite Solar Cell

Yixiong Ji, Wangxian Chen, Di Yan, James Bullock, Yang Xu, Zhenghua Su, Wentong Yang, Jamie Stuart Laird, Tian Zheng, Na Wu, Wusong Zha, Qun Luo, Chang-Qi Ma, Trevor A. Smith, Fangyang Liu, and Paul Mulvaney**

Photovoltaic thin film solar cells based on kesterite $Cu_2ZnSn(S, Se)_4$ (CZTSSe) have reached 13.8% sunlight-to-electricity conversion efficiency. However, this efficiency is still far from the Shockley-Queisser radiative limit and is hindered by the significant deficit in open circuit voltage (V_{OC}). The presence of high-density interface states between the absorber layer and buffer or window layer leads to the recombination of photogenerated carriers, thereby reducing effective carrier collection. To tackle this issue, a new window structure ZnO/AgNW/ZnO/AgNW (ZAZA) comprising layers of ZnO and silver nanowires (AgNWs) is proposed. This structure offers a simple and low-damage processing method, resulting in improved optoelectronic properties and junction quality. The ZAZA-based devices exhibit enhanced V_{OC} due to the higher built-in voltage (V_{bi}) and reduced interface recombination compared to the usual indium tin oxide (ITO) based structures. Additionally, improved carrier collection is demonstrated as a result of the shortened collection paths and the more uniform carrier lifetime distribution. These advances enable the fabrication of the first ITO-free CZTSSe solar cells with over 10% efficiency without an anti-reflective coating.

1. Introduction

Successive power-conversion-efficiency (PCE) breakthroughs over the past several years have brought $Cu_2ZnSn(S, Se)_4$ to the forefront of solar energy research. Although $Cu_2ZnSn(S, Se)_4$ is non-toxic, exhibits excellent photostability, and can be fabricated scaleably and cheaply, these advantages have been overshadowed by its low PCE. The bandgap of kesterite can be tuned over a wide range from 1.0 to 1.5 eV, and it has a very high absorption coefficient, which leads to a theoretical maximum efficiency of around 30%. However, the champion efficiency of 14.9% still lies well behind the efficiency of its counterpart Cu(In, Ga)Se_2 (CIGS) (currently 23.5%[1]) despite the similar electronic structure and device architecture.[2,3]

A major challenge is improving the structure of the upper interfaces between CZTS, the window layer CdS and the transparent conductor, ITO. The CZTS-CdS p-n heterojunction is affected by poor band alignment (conduction band offset), and suboptimal optoelectronic properties of the adjacent transparent conducting films.[4,5]

Hao et al. demonstrated that high-temperature annealing of a CZTS/CdS structure improved the conduction band alignment and minority carrier lifetime within the depletion region.[6] Su et al. likewise found that indium diffusion from the indium tin oxide (ITO) layer caused by annealing, resulted in better carrier equilibration on both sides of the p-n junction and improved the PCE for a Cd-doped CZTS solar cell.[7] Impressively, Xin et al. achieved 13% CZTSSe

Y. Ji, Y. Xu, J. S. Laird, N. Wu, T. A. Smith, P. Mulvaney
ARC Centre of Excellence in Exciton Science
School of Chemistry
University of Melbourne
Victoria 3010, Australia
E-mail: mulvaney@unimelb.edu.au

W. Chen, W. Yang, F. Liu
School of Metallurgy and Environment
Central South University
Changsha 410083, China
E-mail: liufangyang@csu.edu.cn

The ORCID identification number(s) for the author(s) of this article can be found under https://doi.org/10.1002/smll.202307242

© 2023 The Authors. Small published by Wiley-VCH GmbH. This is an open access article under the terms of the Creative Commons Attribution-NonCommercial License, which permits use, distribution and reproduction in any medium, provided the original work is properly cited and is not used for commercial purposes.

DOI: 10.1002/smll.202307242

D. Yan, J. Bullock
Department of Electrical and Electronic Engineering
University of Melbourne
Victoria 3010, Australia

Z. Su
Shenzhen Key Laboratory of Advanced Thin Films and Applications
College of Physics and Optoelectronic Engineering
Shenzhen University
Shenzhen 518060, China

T. Zheng
The Materials Characterisation and Fabrication Platform
Department of Chemical Engineering
University of Melbourne
Victoria 3010, Australia

W. Zha, Q. Luo, C.-Q. Ma
i-Lab & Printable Electronics Research Center
Suzhou Institute of Nano-Tech and Nano-Bionics
Chinese Academy of Sciences (CAS)
Suzhou 215123, China

solar cells by introducing Ag doping and preparing ITO at high temperatures.[8] The resulting change in carrier concentration due to element diffusion in the top layer material significantly improved cell performance. This indicates that the structure of the top window layers has a large impact on overall device performance; however this is not easily captured by conventional evaluation metrics such as window layer transparency and conductivity.

Consequently, a meticulously optimized post-annealing process for the ITO layer is always needed to guarantee the high performance of kesterite solar cells.[7] Typically, the doping density of the ITO film is determined by the density of oxygen vacancies. The indium ions within the ITO may diffuse into the CdS or CZTS layers, leading to changes in the doping concentration of electrons and holes, respectively. Moreover, the n-type dopant concentration within the ITO film is significantly higher than in the CdS layer. Therefore, the ITO film serves not only as a transparent conductive oxide (TCO) but also as a crucial n-type semiconductor in CZTS heterojunction solar cells, whereas the CdS functions more as a buffer layer. Consequently, all aspects of the ITO film, including its conductivity, carrier concentration, mobility, transmittance, and even work function, critically affect the power conversion efficiency of solar cells. Unfortunately, optimizing all of these parameters is challenging due to variations in deposition equipment used across different laboratories. Finally, the increasing scarcity of indium makes replacing it as the TCO increasingly important.

In response to these challenges, we propose a ZnO/AgNW/ZnO/AgNW (ZAZA) transparent electrode structure for kesterite solar cells. This structure is created by combining low-power sputtering and solution processing, offering simplicity and excellent reproducibility. The deposition of the ZAZA top window layer minimizes crystal damage and the number of defects at the CZTSSe/CdS heterojunction by avoiding the prolonged high-power, plasma-assisted sputtering needed for ITO deposition. Additionally, the ZAZA design increases the carrier density without requiring oxygen control or post-treatment. This leads to a higher built-in potential and expanded depletion region with the CZTSSe absorber. Moreover, the carrier collection path is significantly reduced from 400 to 80 nm, and defects near the CZTSSe/CdS interface are eliminated. As a result, the open-circuit voltage (V_{OC}) is improved from 470 mV to over 504 mV, even in the absence of added dopants in the absorber layer.

2. Results and Discussion

The optoelectronic performance of the TCO is usually quantified using the figure of merit (FoM), defined as $\sigma_{dc}/\sigma_{op}(\lambda)$ in the equation:[9]

$$T = \left(1 + \frac{Z_0\sigma_{op}(\lambda)}{2R_{sheet}\sigma_{dc}}\right)^{-2} \quad (1)$$

where Z_0 is the impedance of free space, σ_{dc} and $\sigma_{op}(\lambda)$ are the direct-current and optical conductivities of the materials, respectively, T is the transmittance of the TCO films (measured at a wavelength of 550 nm), and R_{sheet} is the sheet resistance. The value of $FoM = \sigma_{dc}/\sigma_{op}(\lambda)$ can be obtained from Equation (1). However, the calculation of the FoM from the properties of the TCO films alone will lead to an overestimation of the TCO efficiency. The high transmission and conductivity achieved by AgNWs do not guarantee good performance since this also requires good electronic contact with the neighboring layers in the cell. For silver nanowires, the lower contact area and unavoidable roughness of the wire matrix make it difficult to achieve significant improvement in devices even if the material exhibits better transmission and sheet resistance compared to ITO.[10]

To achieve optimal electrical contact, we explored two ZnO and AgNW stacking transparent electrodes, which are shown in **Figure 1**. Compared to ZnO/ITO layers prepared by sputtering, AgNWs spun onto ZnO droop across the large kesterite grains, resulting in poor contact over the valley regions. Because of the higher carrier recombination rate in these regions, ZnO/AgNW-based devices suffer inefficient extraction of charge carriers, resulting in non-uniform surface charge collection for the corresponding solar cells.[11] We found that a ZnO/AgNW/ZnO/AgNW multi-layer composite structure overcomes the above problem. The first ZnO layer was deposited on CdS with a thickness of 30 nm. Then 2mg ml^{-1} AgNWs were spin-coated at 3000 rpm for 40 s and dried at $120^{o}C$ for 15 min. Subsequently, the aforementioned two steps were repeated to create the ZAZA structure. Surprisingly, the deposition of a second layer of 30 nm-ZnO helped push the spin-coated AgNWs deeper into the trenches between the kesterite grains (shown in Figure 1 c2,c3) and dramatically improved the quality of the electrical contact.[9,12] Moreover, when combined with the upper layer of AgNWs, a conductive network was formed, as shown in Figure S1 (Supporting Information). This facilitated enhanced charge extraction at the CZTSSe grain boundary areas and also converted the intrinsic ZnO into a more conductive, n-type semiconductor material.

Photocurrent mapping with contact-mode conductive AFM (c-AFM) was employed to study the current collection efficiency of the devices with both ZnO/ITO and ZAZA structures. To match the 0–3 nA measurement range of the c-AFM electronics, a weak LED was used to illuminate the solar cell, and a resistor was connected in series to enable the detection of the photogenerated current (**Figure 2**a).[13,14] Typical topography and surface photocurrent maps are presented in Figure 2b–e. During the measurements, the tip was grounded and a positive 0.3 V bias was applied to the sample. The disparity in the current collection at grain-in (GI) and grain-boundary (GB) sites is evident in c-AFM mapping. The ZnO/ITO configuration is capable of efficient collection of the photocurrent generated at GIs, while the extraction at the GBs is comparatively poor. By studying the current collection across both smooth and rough areas of the device, the role of surface roughness can be taken into account. Importantly, in the ZAZA sample, the bent silver nanowires enable the carriers to be efficiently extracted even at the grain boundaries. This suggests that better photovoltaic performance can be achieved in ZAZA-based solar cells.

The photovoltaic performance parameters of CZTSSe devices with ZnO/AgNW/ZnO/AgNW and ZnO/ITO window structures, including open circuit voltage (V_{OC}), short-circuit current density (J_{SC}), fill factor (FF), and power conversion efficiency (PCE) are shown in **Figure 3**. Devices with a ZAZA window structure

© 2023 The Authors. Small published by Wiley-VCH GmbH

16136829, 0, Downloaded from https://onlinelibrary.wiley.com/doi/10.1002/smll.202307242 by Suzhou Institute Of Nano-Tech, Wiley Online Library on [15/01/2024]. See the Terms and Conditions (https://onlinelibrary.wiley.com/terms-and-conditions) on Wiley Online Library for rules of use; OA articles are governed by the applicable Creative Commons License

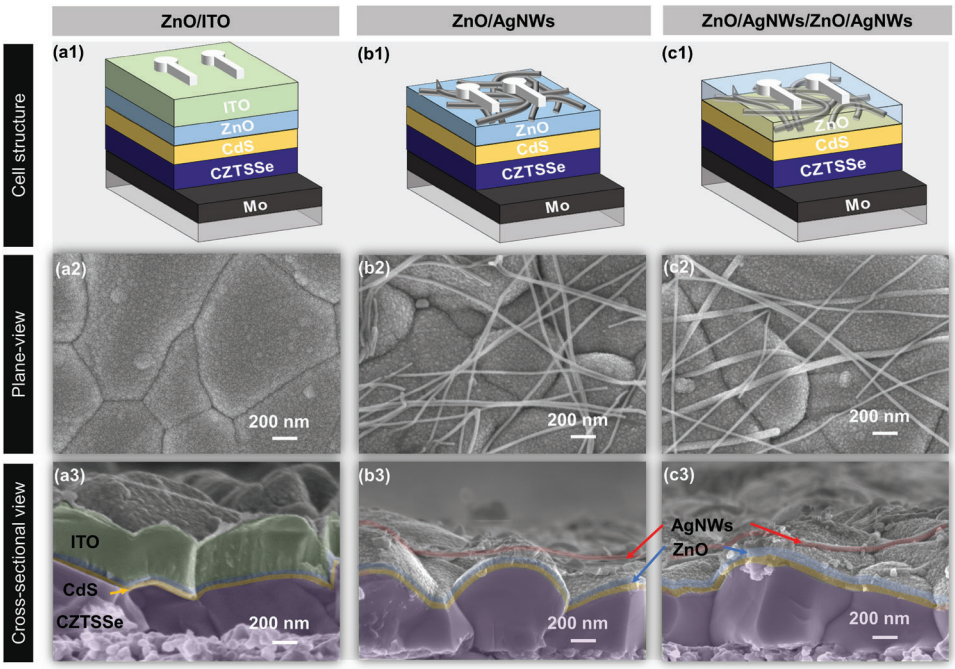

Figure 1. Device structures with different window layers: a1) Mo/CZTSSe/CdS/ZnO/ITO (denoted as 'ZITO'), b1) Mo/CZTSSe/CdS/ZnO/AgNW (denoted as 'ZA'), and c1) Mo/CZTSSe/CdS/ZnO/AgNW/ZnO/AgNW (denoted as 'ZAZA'). The corresponding plane-view SEM images of ZITO, ZA, and ZAZA devices are shown in (a2,b2,c2) and the cross-sectional SEM images are shown in (a3,b3,c3).

exhibit a clear and significant improvement in V_{OC}, but an insignificant improvement in current density, which is not what we expected, based on the c-AFM results. To better comprehend this phenomenon, a more detailed analysis of two champion devices is presented in **Table 1**. The final current density and fill factor were not substantially increased due to higher series resistance, potentially stemming from insufficient element diffusion of the absorbers, resulting in decreased carrier density and reduced conductivity. However, consistent with our expectations, the shunt resistance was notably enhanced due to more efficient

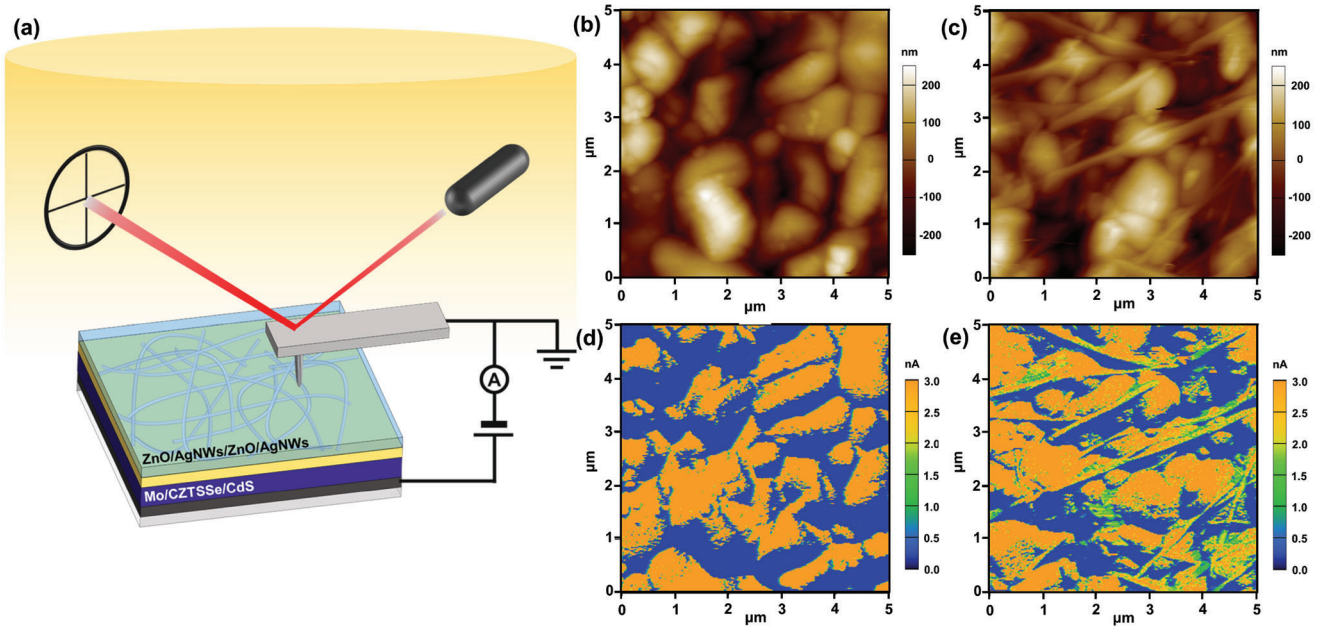

Figure 2. a) Set-up for conductive AFM mapping under weak illumination. Topography and conductive AFM mapping of ZITO device (b,d) and ZAZA device (c,e), respectively.

© 2023 The Authors. Small published by Wiley-VCH GmbH

16136829, 0, Downloaded from https://onlinelibrary.wiley.com/doi/10.1002/smll.202307242 by Suzhou Institute Of Nano-Tech, Wiley Online Library on [15/01/2024]. See the Terms and Conditions (https://onlinelibrary.wiley.com/terms-and-conditions) on Wiley Online Library for rules of use; OA articles are governed by the applicable Creative Commons License

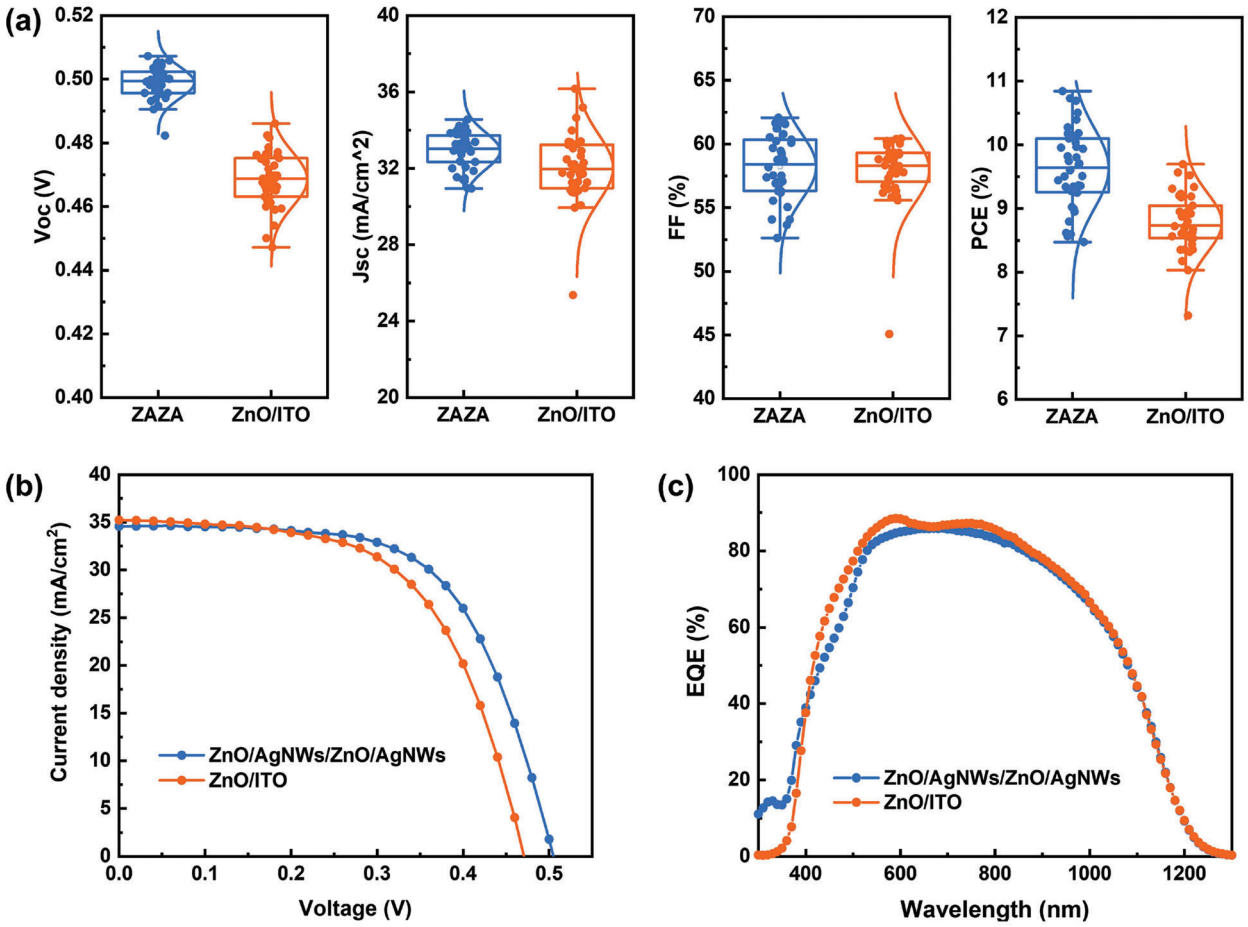

Figure 3. a) Plots of the V_{oc}, J_{sc}, FF, and power conversion efficiency for 38 independent ZITO and ZAZA solar cells. b,c) *J–V* curves and EQE spectra for the champion ZITO and ZAZA devices, respectively.

electron collection from the ZAZA structure. This supports our hypothesis that by avoiding ITO deposition, we can minimize the likelihood of shunting and obviate the creation of plasma-induced defects.

The V_{OC} in a thin-film solar cell is determined by the built-in potential across the p-n junction, which is a function of the carrier densities on both the n and p sides, as shown in Equation (2). Here k is the Boltzmann constant, T is the temperature, and q is the elementary charge. N_D represents the donor densities in CdS, ZnO, ITO, or ZAZA layers, and N_A represents the acceptor density in the CZTSSe layer. The change in V_{bi} caused by the n-side carrier density difference is described by Equation (3). Hall measurements on ZnO/ITO and ZAZA electrodes were used to determine the carrier densities (see Figure S2, Supporting Information). The ZAZA structure exhibited a much higher n-type doping concentration (of approximately 10^{24} cm^{-3}) than the ZnO/ITO films (10^{21} cm^{-3}), which led to an increased built-in potential, resulting in greater band bending and increased V_{OC} at the heterojunction. A similar phenomenon has been observed in previous studies of CIGS and CZTS solar cells by using Ag-NWs in place of ITO (as listed in Tables S1 and S2, Supporting Information): a higher open circuit voltage is often achieved using the AgNW-based structure.[15–26] Here, we attribute this phenomenon to the neglected carrier density enhancement of the ZnO window layer with embedded AgNW conductive frameworks.[27]

$$V_{bi} = \frac{kT}{q} ln \frac{N_D \times N_A}{N_i^2} \quad (2)$$

Table 1. The photovoltaic and diode parameters of the best ZAZA and ZITO solar cells. The values of E_g are obtained from the EQE data. The diode parameters are extracted from dark *J–V* curves.

Device	V_{OC} (V)	J_{SC} (mA cm^{-2})	FF (%)	PCE (%)	A	J_0 (mA cm^{-2})	R_S (ohm cm^2)	G_{SH} (mS cm^{-2})	Eg/q-V_{OC} (eV)	E_U (meV)
ZAZA	0.504	34.6	62.8	10.8	1.49	3.37×10^{-5}	1.83	0.036	0.596	47.3
ZITO	0.470	35.2	60.0	9.7	1.82	8.90×10^{-4}	1.52	0.282	0.63	45.8

© 2023 The Authors. Small published by Wiley-VCH GmbH

16136829, 0, Downloaded from https://onlinelibrary.wiley.com/doi/10.1002/smll.202307242 by Suzhou Institute Of Nano-Tech, Wiley Online Library on [15/01/2024]. See the Terms and Conditions (https://onlinelibrary.wiley.com/terms-and-conditions) on Wiley Online Library for rules of use; OA articles are governed by the applicable Creative Commons License

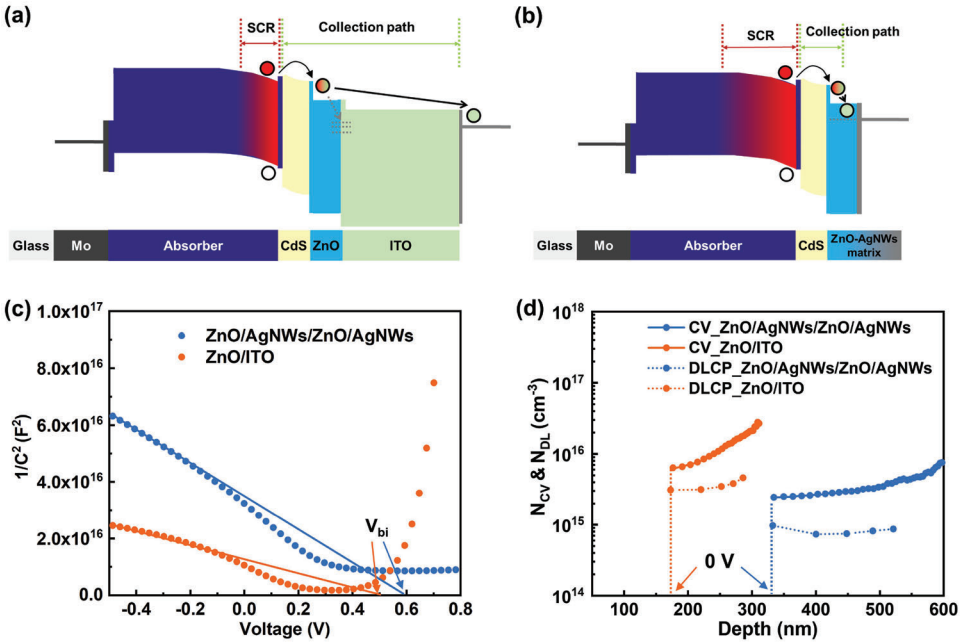

Figure 4. Schematic diagrams of carrier extraction in a) ZITO and b) ZAZA devices. c) Plot of $1/C^2$ versus voltage showing the variation in the built-in potential, V_{bi}. d) CV-DLCP curves and the calculated width of the space charge region are shown as the dashed lines at 0 V bias.

$$\Delta V_{bi} = \frac{kT}{q} ln \frac{N_D^{CdS+ZAZA}}{N_D^{CdS+ZnO/ITO}} \quad (3)$$

$$N_{CV} = \frac{-\varepsilon_{r,n} N_D}{(d((1/C^2))/dV) q A^2 \varepsilon_0 \varepsilon_{r,n} N_D + 2\varepsilon_{r,p}} \quad (4)$$

$$N_{DLCP} = -\frac{C_0^3}{2qA^2\varepsilon_0\varepsilon_{r,p}C_1} \quad (5)$$

In addition to considering the built-in potential within the junction, we have conducted defect analysis on the performance of the heterojunction with and without the high-energy plasma process using both capacity–voltage (*C–V*) profile and drive-level capacity profile (DLCP) measurements (**Figure 4**). The charge density, width of the depletion region, and defect densities derived from *C–V* and DLCP data are listed in **Table 2**. Based on the *C–V* data, the built-in potential of the p-n junction was increased from 0.50 V for the ITO-based device to 0.58 V for the ZAZA device. N_{DL}-derived DLCP measurements include responses from both the free carriers in CZTSSe and any deep-level defects, while the N_{CV} from *C–V* also includes the response from interface trap states.[28] It is noticeable that both the N_{CV} and N_{DL} responses for the devices with ZAZA structure are decreased significantly, even though identical processes were used to prepare the kesterite absorber layers. The differences in free carrier concentration, therefore, arise from differences in the fabrication processes for the top TCO layers. We believe this results in differing amounts of atomic diffusion across the interfaces during the processing. The lack of atomic Indium is the main reason for the relatively lower carrier concentration in the ZAZA sample.[7] In addition, the disparity between the *C–V* and DLCP measurements at zero bias is likely due to the presence of interface traps within the junction. A decrease in the N_{CV}-N_{DL} values at zero bias indicates a reduction in the number of interface traps present at the CZTSSe/CdS junction (Table 2).

Sun-V_{OC} measurements are an effective method for analyzing heterojunction quality and were performed on the champion ZAZA device with a ZITO device serving as the reference. We assumed that J_{SC} is proportional to the light intensity (Equation (6)).[29] The ideality factors that directly reflect the performance of a diode can be extracted from the Suns-V_{OC} curves as shown in **Figure 5**. The ZAZA device exhibited consistently better diode properties (i.e., a lower ideality factor) from low injection levels right up to high injection levels.

$$\text{Suns} = \frac{J_L(\text{light intensity})}{J_{SC}(\text{one sun})} \quad (6)$$

$$J = J_L - J_{01}\left(\exp\left(\frac{V_{oc}}{V_T}\right) - 1\right) - J_{02}\left(\exp\left(\frac{V_{oc}}{2V_T}\right) - 1\right) - \frac{V_{oc}}{R_{sh}} \quad (7)$$

Table 2. Summary of the results derived from C–V and DLCP measurements.

Device	V_{bi}(V)	N_{CV}(cm^{-3})	N_{DL}(cm^{-3})	Depletion width(nm)	Interface state response(relative values)
ZAZA	0.58	2.44×10^{15}	9.74×10^{14}	332	1.46×10^{15}
ZITO	0.50	6.33×10^{15}	3.09×10^{15}	172	3.24×10^{15}

© 2023 The Authors. Small published by Wiley-VCH GmbH

16136829, 0, Downloaded from https://onlinelibrary.wiley.com/doi/10.1002/smll.202307242 by Suzhou Institute Of Nano-Tech, Wiley Online Library on [15/01/2024]. See the Terms and Conditions (https://onlinelibrary.wiley.com/terms-and-conditions) on Wiley Online Library for rules of use; OA articles are governed by the applicable Creative Commons License

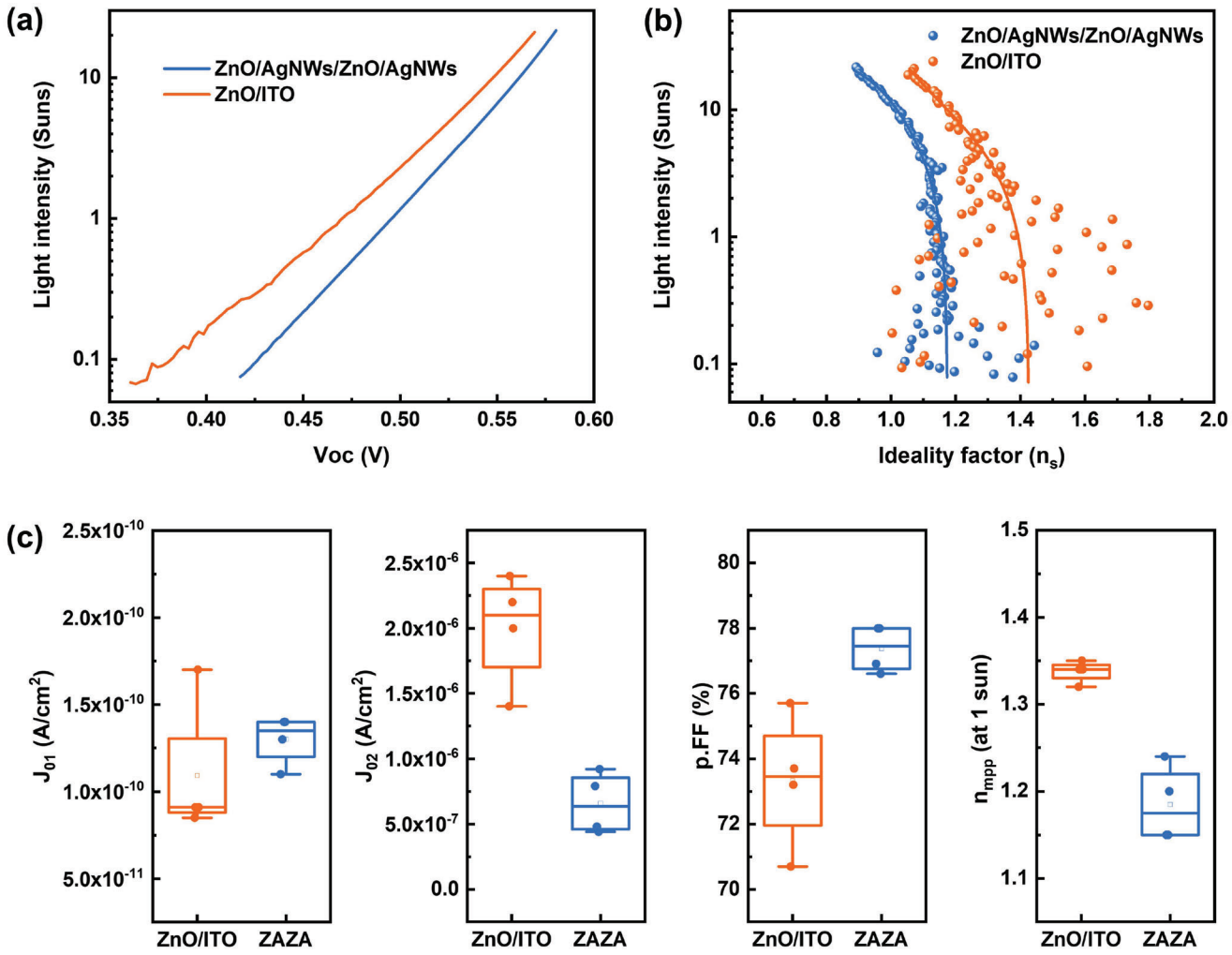

Figure 5. a) Light intensity versus V_{OC} for ZAZA and ZITO devices. b) Ideality factor n_s as a function of light intensity. c) Device performance parameters by fitting Suns-V_{OC} curves using a two-diode model.

The recombination parameters were extracted from the obtained Sun-V_{OC} data using the usual two-diode model in Equation (7). Here, V_T is the thermal voltage, and J_{01} and J_{02} are the saturation currents for the $n = 1$ and $n = 2$ diodes, respectively. Typically, J_{01} is determined primarily by the rate of recombination within the neutral zone of the CZTSSe absorber, i.e., deeper within the absorber layer, while J_{02} represents the recombination within the space charge region (SCR) which lies closer to the heterojunction.[30] It is noteworthy that while J_{01} remains almost unchanged, J_{02} experiences a significant decrease for cells with the ZAZA structure, suggesting that recombination within the SCR is drastically reduced. Moreover, there is a higher pseudo-FF and better n_{mpp} that are consistent with higher p-n junction diode quality and/or decreased defect concentration at the CZTSSe/CdS interface.[6]

To further understand the carrier recombination mechanisms at the heterojunction interface of ZnO/ITO and ZAZA devices, time-resolved emission microscopy (TREM) with a submicrometer resolution was carried out. It is worth noticing that a 532 nm laser was used to excite the PL signal at a shallow depth through the whole CZTSSe absorber so that more information about the interface and quality of the SCR could be collected. The ZAZA and ZITO devices present comparable average lifetimes (τ_m) of 3.40 and 3.38 ns, respectively, as shown in Figure S7 (Supporting Information). The TREM results in **Figure 6** provide additional details regarding the uniformity of lifetimes, including the average lifetime τ_m, and the biexponential fitted lifetimes τ_1 and τ_2. In general, τ_1 represents the fast decay time of photogenerated carriers, which is mainly due to the interface recombination and defects in the shallow depth of the material. τ_2 represents the slow decay time, which is related to bulk recombination and can be used to evaluate the quality of the bulk absorbers.[31] Specifically, an overall longer τ_1 from the ZAZA device indicates a better CZTSSe/CdS interface and also improved junction quality. Conversely, a shorter τ_2 is also evident for the same device, which results from insufficient dopant interdiffusion within the low-energy processed ZAZA solar cells. The uniformity of lifetimes is displayed in tau

© 2023 The Authors. Small published by Wiley-VCH GmbH

16136829, 0, Downloaded from https://onlinelibrary.wiley.com/doi/10.1002/smll.202307242 by Suzhou Institute Of Nano-Tech, Wiley Online Library on [15/01/2024]. See the Terms and Conditions (https://onlinelibrary.wiley.com/terms-and-conditions) on Wiley Online Library for rules of use; OA articles are governed by the applicable Creative Commons License

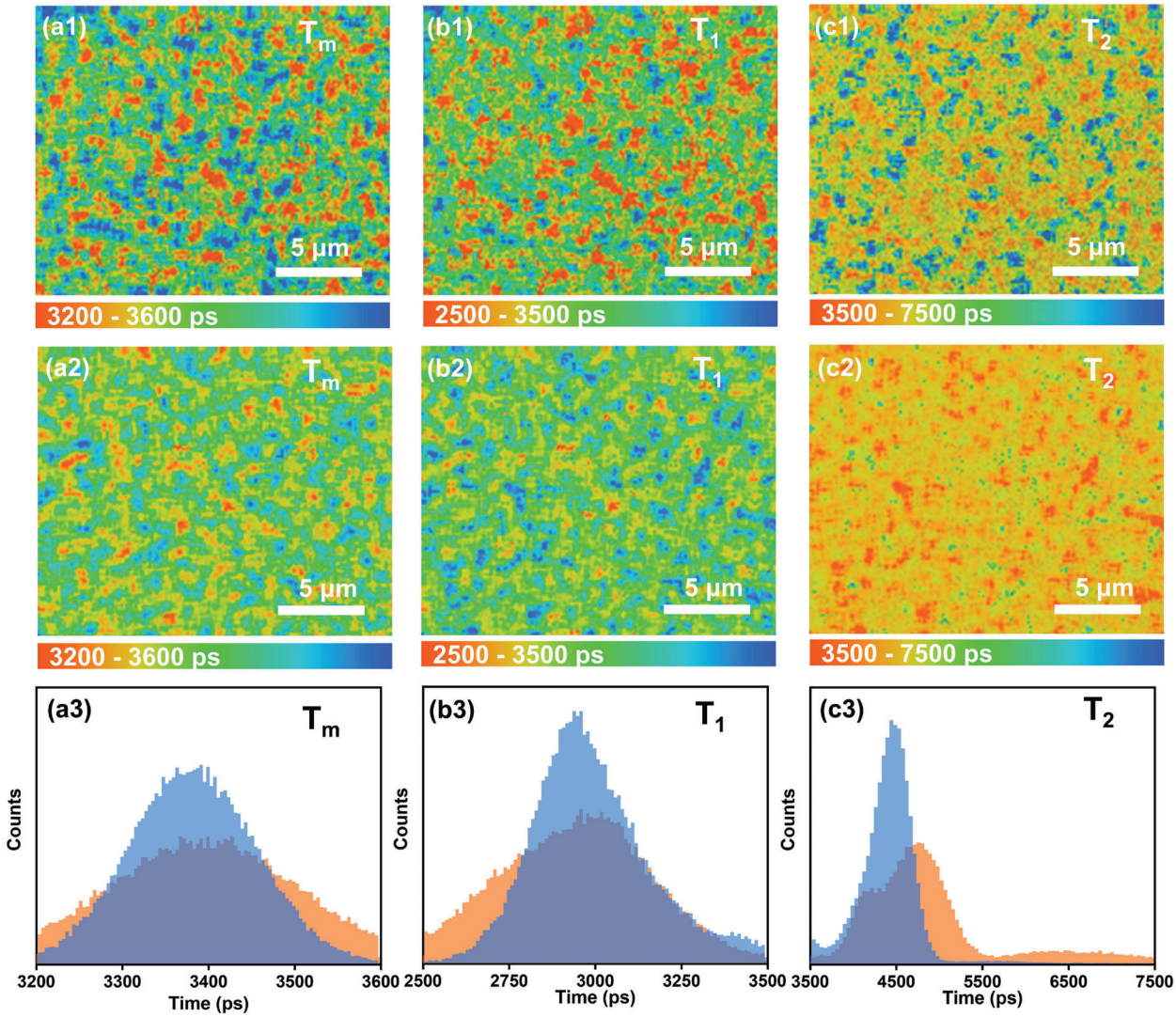

Figure 6. Time-resolved emission microscopy (TREM) images of the ZITO and ZAZA devices. In (a1,b1,c1), the average lifetimes (τ_m), fitted fast decay times τ_1, and slow decay times τ_2 are shown for the ZITO device. (a2,b2,c2) display the respective values for the ZAZA device. Tau plots of the corresponding lifetimes are depicted in (a3) for τ_m, (b3) for τ_1, and (c3) for τ_2, with blue shadows for the ZAZA device and orange shadows for the ZITO device.

plots, indicating obvious improvements in devices with the ZAZA structure.

3. Conclusion

An AgNW-based ZnO/AgNW/ZnO/AgNW window structure has been proposed as a replacement for ITO in kesterite solar cells. Due to the increased carrier density and the avoidance of high-energy sputtering, an enlarged built-in potential and better junction quality have been attained. The new window layer exhibits decreased interface recombination. The open circuit voltage has been improved from 0.470 V to over 0.504V without any doping or post-treatment. The data clearly illustrate that the V_{OC} deficit in kesterite solar cells can be drastically reduced through better device architectures.

4. Experimental Section

Reagent and Materials: $Cu(CH_3COO)_2H_2O$ (99.99%), $ZnCl_2$ (99.99%), $SnCl_22H_2O$ (99.99%), thiourea (99.999%), $CdSO_48/3H_2O$ (99.99%), and 2-methoxyethanol (99.8%) were purchased from Aladdin. Ammonium hydroxide (25.0–28.0%) was from Sinopharm Chemical Reagent Co. Ltd. AgNW was purchased from Blue Nano with an average diameter of 20 nm and 15 μm in length. The AgNW dispersion was diluted to 2 mg mL^{-1} with ethanol before spin coating. Mo-coated glasses were purchased from Suzhou Shangyang Solar Technology Co., Ltd.

CZTSSe Absorber: The CZTS precursor solution was fabricated by dissolving $Cu(CH_3COO)_2$ H_2O (0.28 mol L^{-1}), $ZnCl_2$ (0.2 mol L^{-1}), $SnCl_2$ $2H_2O$ (0.17 mol L^{-1}), and thiourea (1.33 mol L^{-1}) into 2-methoxyethanol. The solution was kept stirred until the color of the final solution was pale yellow. The precursor solution was spin-coated onto Mo-coated glass at 3000 rpm for 40 s, followed by baking at 280 °C for 2 min. The above steps were repeated several times to fabricate 1.5 μm

© 2023 The Authors. Small published by Wiley-VCH GmbH

16136829, 0, Downloaded from https://onlinelibrary.wiley.com/doi/10.1002/smll.202307242 by Suzhou Institute Of Nano-Tech, Wiley Online Library on [15/01/2024]. See the Terms and Conditions (https://onlinelibrary.wiley.com/terms-and-conditions) on Wiley Online Library for rules of use; OA articles are governed by the applicable Creative Commons License

precursor films. Then, selenization was carrried outat 550°C for 10 min in a rapid thermal process (RTP) furnace to form the final CZTSSe absorbers.[32]

Device Fabrication: The architectures of all samples are listed below:
ZITO device: Glass/Mo/CZTSSe/CdS/ZnO (60 nm)/ITO/Ag.
ZA device: Glass/Mo/CZTSSe/CdS/ZnO (60 nm)/AgNW/Ag.
ZAZA device: Glass/Mo/CZTSSe/CdS/ZnO (30 nm)/AgNW/ZnO (30 nm)/AgNW/Ag.

Specifically, the selenized films were immersed into a solution mixed with 150 ml DI water, 20 ml 0.015 mol L^{-1} $CdSO_4$ solution, 20 ml 0.75 mol L^{-1} thiourea solution, and 25 ml ammonium hydroxide at 75°C to complete the deposition of the 50 nm CdS buffer layer. Next, 60 nm i-ZnO and 300 nm ITO were sequentially magnetron-sputtered on the top of the buffer layer to complete the fabrication of the ZITO device. ITO was replaced by AgNW in ZA devices. Spin-coating 2 mg ml^{-1} AgNW at 3000 rpm twice (baking at 120 °C for 15 min after each coating) yields layers with a similar conductivity and transmission to ITO. For ZAZA devices, 30 nm ZnO was sputtered first, then AgNWs were spin-coated on top. This was then repeated to create the ZAZA structure. Finally, 300 nm Ag grids were thermally evaporated as a top electrode. No antireflection layer was used. All the devices were mechanically cut to yield active device areas of 0.24 cm^2.

Characterization: Top-view and cross-sectional images were collected using a JEOL JSM-7900F field emission scanning electron microscope (FESEM). The acceleration voltage was 5 kV. The electrical properties of the thin films were measured using a Hall-effect measurement system (HL5500PC, 200 Nanometrics). C-AFM images were acquired with a Cypher ES AFM (Asylum Research, US) atomic force microscope using an ORCA holder and a conductive cantilever (ASYELEC 01-R2, spring constant = 2.8 N/m). The tip bias was set to 0.3 V for all the samples and a scan size of 5 µm. Topography and current images were acquired simultaneously. The *J–V* characteristics of CZTSSe devices were measured using a Xenon-lamp-based solar simulator (Newport, AM 1.5G, 100 mW cm^{-2}) in conjunction with a Keithley 2400 SourceMeter. The external quantum efficiencies (EQE) were measured using a QE-R measurement system (Enli Tech) and were calibrated using Enli Tech. Lab-certified Si and Ge reference photodiodes. The capacitance–voltage (*C–V*) measurements were performed with an impedance analyzer at a frequency of 100 kHz with a DC bias voltage sweeping from −1.0 to 0.8 V. Drive-level capacitance profiling (DLCP) measurements were carried out using AC amplitudes varying from 40 to 140 mV and with DC bias voltages that swept from −1.0 to 0.8 V. Suns-*Voc* measurements were collected using a Sinton Instrument, which combines the Suns-*Voc* stage and a WCT-120 lifetime testing instrument. The measurements were carried out at room temperature. The instrument employed a Xenon flashlamp as the light source. To investigate the minority lifetime, time-resolved photoluminescence measurements were conducted. Samples were excited at 532 nm with a super-continuum laser (SuperK Extreme, NKT) operating at 78 MHz. Fluorescence decay and TREM images were collected with a high NA objective (UplanApo 100X, NA = 1.4, Olympus) on a scanning confocal microscope (Fluoview 300, IX71, Olympus). To time-resolve the photoluminescence of the samples, emission signals from the sample were detected using a single-photon counting photomultiplier tube (SPC-150, Becker and Hickl). Fluorescence decay data collection and analysis were monitored and processed by PC-installed software packages (bh-SPCM and SPCImage, Becker and Hickl).

Supporting Information

Supporting Information is available from the Wiley Online Library or from the author.

Acknowledgements

Y.J. and W.C. contributed equally to this work. This work was funded by the National Key Research and Development Program of China (2018YFE0203400) and the ARC Centre of Excellence in Exciton Science through ARC Grant CE170100026. The authors acknowledge support from DIISR through the Australia-China Science Research Fund (Grant ACSRIII000001). Yixiong Ji wants to thank Dr.Sergey Rubanov for his help with FIB and TEM, Claire Dawson for AgNW synthesis, and Trent Ralph for his support with the RTP furnace set-up.

Open access publishing facilitated by The University of Melbourne, as part of the Wiley - The University of Melbourne agreement via the Council of Australian University Librarians.

Conflict of Interest

The authors declare no conflict of interest.

Data Availability Statement

The data that support the findings of this study are available from the corresponding author upon reasonable request.

Keywords

ITO free, low-damage, window structure, kesterite, photovoltaics

Received: August 31, 2023
Revised: September 10, 2023
Published online:

[1] M. Nakamura, K. Yamaguchi, Y. Kimoto, Y. Yasaki, T. Kato, H. Sugimoto, *IEEE J. Photovoltaics* **2019**, *9*, 1863.
[2] J. Zhou, X. Xu, H. Wu, J. Wang, L. Lou, K. Yin, Y. Gong, J. Shi, Y. Luo, D. Li, H. Xin, Q. Meng, *Nat. Energy* **2023**, *8*, 526.
[3] Z. Wang, J. Guo, Y. Pan, J. Fang, C. Gong, L. Mo, Q. Luo, J. Lin, C. Ma, **2023**, https://doi.org/10.1002/eem2.12592.
[4] K. Sun, C. Yan, F. Liu, J. Huang, F. Zhou, J. A. Stride, M. Green, X. Hao, *Adv. Energy Mater.* **2016**, *6*, 1600046.
[5] F. Liu, C. Yan, J. Huang, K. Sun, F. Zhou, J. A. Stride, M. A. Green, X. Hao, *Adv. Energy Mater.* **2016**, *6*, 1600706.
[6] C. Yan, J. Huang, K. Sun, S. Johnston, Y. Zhang, H. Sun, A. Pu, M. He, F. Liu, K. Eder, L. Yang, J. M. Cairney, N. J. Ekins-Daukes, Z. Hameiri, J. A. Stride, S. Chen, M. A. Green, X. Hao, *Nat. Energy* **2018**, *3*, 764.
[7] Z. Su, G. Liang, P. Fan, J. Luo, Z. Zheng, Z. Xie, W. Wang, S. Chen, J. Hu, Y. Wei, C. Yan, J. Huang, X. Hao, F. Liu, *Adv. Mater.* **2020**, *32*, 2000121.
[8] Y. Gong, Q. Zhu, B. Li, S. Wang, B. Duan, L. Lou, C. Xiang, E. Jedlicka, R. Giridharagopal, Y. Zhou, Q. Dai, W. Yan, S. Chen, Q. Meng, H. Xin, *Nat. Energy* **2022**, *7*, 966.
[9] Y. Sun, M. Chang, L. Meng, X. Wan, H. Gao, Y. Zhang, K. Zhao, Z. Sun, C. Li, S. Liu, H. Wang, J. Liang, Y. Chen, *Nat. Electron.* **2019**, *2*, 513.
[10] G. Zeng, W. Chen, X. Chen, Y. Hu, Y. Chen, B. Zhang, H. Chen, W. Sun, Y. Shen, Y. Li, F. Yan, Y. Li, *J. Am. Chem. Soc.* **2022**, *144*, 8658.
[11] J. Li, J. Huang, F. Ma, H. Sun, J. Cong, K. Privat, R. F. Webster, S. Cheong, Y. Yao, R. L. Chin, X. Yuan, M. He, K. Sun, H. Li, Y. Mai, Z. Hameiri, N. J. Ekins-Daukes, R. D. Tilley, T. Unold, M. A. Green, X. Hao, *Nat. Energy* **2022**, *7*, 754.
[12] Z. Wang, J. Guo, Y. Pan, J. Fang, C. Gong, L. Mo, Q. Luo, J. Lin, C. Ma, *Energy Environ. Mater.* **2023**, e12592.
[13] J. B. Li, V. Chawla, B. M. Clemens, *Adv. Mater.* **2012**, *24*, 720.
[14] A. Kim, Y. Won, K. Woo, S. Jeong, J. Moon, *Adv. Funct. Mater.* **2014**, *24*, 2462.

© 2023 The Authors. Small published by Wiley-VCH GmbH

16136829, 0, Downloaded from https://onlinelibrary.wiley.com/doi/10.1002/smll.202307242 by Suzhou Institute Of Nano-Tech, Wiley Online Library on [15/01/2024]. See the Terms and Conditions (https://onlinelibrary.wiley.com/terms-and-conditions) on Wiley Online Library for rules of use; OA articles are governed by the applicable Creative Commons License

[15] W.-C. Hsu, H. Zhou, S. Luo, T.-B. Song, Y.-T. Hsieh, H.-S. Duan, S. Ye, W. Yang, C.-J. Hsu, C. Jiang, B. Bob, Y. Yang, *ACS nano* **2014**, *8*, 9164.
[16] J. Park, Z. Ouyang, C. Yan, K. Sun, H. Sun, F. Liu, M. Green, X. Hao, *J. Phys. Chem. C* **2017**, *121*, 20597.
[17] A. Teymouri, S. Pillai, Z. Ouyang, X. Hao, F. Liu, C. Yan, M. A. Green, *ACS Appl. Mater. Interfaces* **2017**, *9*, 34093.
[18] Y. Gu, H. Shen, C. Ye, X. Dai, Q. Cui, J. Li, F. Hao, X. Hao, H. Lin, *Adv. Funct. Mater.* **2018**, *28*, 1703369.
[19] Y. Gu, C. Ye, X. Yin, J. Han, Y. Zhou, H. Shen, J. Li, X. Hao, H. Lin, *Chem. Eng. J.* **2018**, *351*, 791.
[20] Y. Gu, X. Yin, J. Han, Y. Zhou, M. Tai, Q. Zhang, J. Li, X. Hao, H. Lin, *ChemistrySelect* **2019**, *4*, 982.
[21] J. Jang, J. S. Lee, K.-H. Hong, D.-K. Lee, S. Song, K. Kim, Y.-J. Eo, J. H. Yun, C.-H. Chung, *Sol. Energy Mater. Sol. Cells* **2017**, *170*, 60.
[22] A. Kim, Y. Won, K. Woo, S. Jeong, J. Moon, *Adv. Funct. Mater.* **2014**, *24*, 2462.
[23] M. Singh, J. Jiu, T. Sugahara, K. Suganuma, *ACS Appl. Mater. Interfaces* **2014**, *6*, 16297.
[24] A. Kim, Y. Won, K. Woo, C.-H. Kim, J. Moon, *ACS nano* **2013**, *7*, 1081.
[25] S. Lee, J. S. Lee, J. Jang, K.-H. Hong, D.-K. Lee, S. Song, K. Kim, Y.-J. Eo, J. H. Yun, J. Gwak, C.-H. Chung, *Nano Energy* **2018**, *53*, 675.
[26] S. Lee, J. Jang, T. Park, Y. M. Park, J. S. Park, Y.-K. Kim, H.-K. Lee, E.-C. Jeon, D.-K. Lee, B. Ahn, C.-H. Chung, *ACS Appl. Mater. Interfaces* **2020**, *12*, 6169.
[27] H. Han, N. Theodore, T. Alford, *J. Appl. Phys.* **2008**, *103*, 013708.
[28] J. T. Heath, J. D. Cohen, W. N. Shafarman, *J. Appl. Phys.* **2004**, *95*, 1000.
[29] O. Gunawan, T. Gokmen, D. B. Mitzi, *J. Appl. Phys.* **2014**, *116*, 084504.
[30] C.-T. Sah, R. N. Noyce, W. Shockley, *Proc. IRE* **1957**, *45*, 1228.
[31] H. Tampo, K. M. Kim, S. Kim, H. Shibata, S. Niki, *J. Appl. Phys.* **2017**, *122*, 023106.
[32] Y. Ji, X. Zhao, Y. Pan, Z. Su, J. Lin, E. M. Akinoglu, Y. Xu, H. Zhang, P. Zhao, Y. Dong, X. Wei, F. Liu, P. Mulvaney, *Adv. Funct. Mater.* **2023**, *33*, 2211421.

© 2023 The Authors. Small published by Wiley-VCH GmbH

16136829, 0, Downloaded from https://onlinelibrary.wiley.com/doi/10.1002/smll.202307242 by Suzhou Institute Of Nano-Tech, Wiley Online Library on [15/01/2024]. See the Terms and Conditions (https://onlinelibrary.wiley.com/terms-and-conditions) on Wiley Online Library for rules of use; OA articles are governed by the applicable Creative Commons License